The Astrophysical Journal, 893:2 (13pp), 2020 April 10 https://doi.org/10.3847/1538-4357/ab7dc2

Gravitational-wave Radiation of Double Degenerates with Extremely Low-mass White Dwarf Companions

Zhenwei Li[1,2,3], Xuefei Chen[1,2,4], Hai-Liang Chen[1,2], Jiao Li[1,2,3], Shenghua Yu[5], and Zhanwen Han[1,2,4]
[1] Yunnan Observatories, Chinese Academy of Sciences, Kunming, 650011, People's Republic of China; cxf@ynao.ac.cn
[2] Key Laboratory for the Structure and Evolution of Celestial Objects, Chinese Academy of Sciences, People's Republic of China
[3] University of the Chinese Academy of Sciences, Yuquan Road 19, Shijingshan Block, 100049, Beijing, People's Republic of China
[4] Center for Astronomical Mega-Science, Chinese Academy of Sciences, 20A Datun Road, Chaoyang District, Beijing 100012, People's Republic of China
[5] National Astronomical Observatories, Chinese Academy of Sciences, Beijing, 100101, People's Republic of China
Received 2019 November 11; revised 2020 February 10; accepted 2020 March 5; published 2020 April 8

Abstract

Double degenerate (DD) systems are supposed to be significant gravitational-wave (GW) sources for future space-based GW detectors, e.g., the Laser Interferometer Space Antenna (LISA). Recently, one type of DD system with extremely low-mass WD (ELM WD; $\lesssim 0.30\,M_{\odot}$) companions was found in the ELM Survey. These companions have very short orbital periods and are therefore important sources for LISA detection. Further, due to the thick envelope of ELM WDs compared with massive WDs (e.g., CO WDs), they are much easier to find through the combination of electromagnetic (EM) and GW observations. In this paper, we first obtain the population of ELM WDs in DDs by considering the detailed evolutionary tracks of ELM WDs and then analyzing the GW radiation of these systems. We found that about 6×10^3 sources could be solely detected by LISA, including $\sim 2 \times 10^3$ chirping sources, and $\sim$13 ($\sim$107) more sources are expected to be detected by both LISA and the ELM Survey (Gaia).

Unified Astronomy Thesaurus concepts: Gravitational waves (678); Close binary stars (254); White dwarf stars (1799)

1. Introduction

Double white dwarfs (DWDs), also known as double degenerates (DDs), are supposed to be dominant sources for the future space-based gravitational-wave (GW) detector, the Laser Interferometer Space Antenna (LISA; Amaro-Seoane et al. 2013, 2017). Binary population synthesis (BPS) studies show that about several 10^7 DWDs exist in our Galaxy. Many DWDs will make contributions to the LISA noise (which is called confusion foreground noise), while $(\sim 1\text{–}3) \times 10^4$ sources are expected to be individually detected by LISA (Evans et al. 1987; Webbink & Han 1998; Nelemans et al. 2001; Liu 2009; Liu et al. 2010; Ruiter et al. 2010; Yu & Jeffery 2010; Nissanke et al. 2012; Korol et al. 2017, 2019; Lamberts et al. 2019, and references therein). Further, a growing number of currently operational or future planned optical telescopes, e.g., the Large Synoptic Survey Telescope (LSST; LSST Science Collaboration et al. 2009), Gaia (Carrasco et al. 2014), etc., will make it possible to detect the electromagnetic (EM) counterparts of GW sources (Cooray et al. 2004; Nelemans 2006; Littenberg et al. 2013; Korol et al. 2017; Kupfer et al. 2018). For example, the recently detected detached DWD ZTF J1539+5027 (ZTF J1539 hereafter) with orbital period of 6.91 minutes, representing the shortest currently known period among detached DWDs, will be identified by LISA with a high signal-to-noise ratio (S/N; Burdge et al. 2019a; Littenberg & Cornish 2019). The multimessenger study of DWDs will allow us to get more precise information from these systems (Shah & Nelemans 2014a, 2014b; Littenberg & Cornish 2019), which could furthermore give a constraint of the Galaxy structure (Korol et al. 2019) and shed light on the physics of mass transfer between DWDs (Baker et al. 2019).

In recent years, Brown and his collaborators have found a large number of DWDs with extremely low-mass (ELM, $\lesssim 0.30\,M_{\odot}$) helium WD companions[6] from the ELM Survey operated on the 6.5 m MMT in SAO (Brown et al. 2010, 2012, 2013, 2016a; Kilic et al. 2011, 2012; Gianninas et al. 2015; Brown et al. 2020). Such DWDs have very short orbital periods and the two most compact, J0651+2844 and J0935+4411 (J0651, J0935 hereafter), are expected to be verification sources[7] for LISA (Brown et al. 2011; Hermes et al. 2012; Brown et al. 2016a; Kupfer et al. 2018). In comparison to relatively massive WDs, ELM WDs have much thicker H-rich envelopes and longer timescales in the proto stage[8] (after the stripping of the envelope and before the extinction of shell burning). This stage is the most luminous stage except for flashes, and the timescales for this phase are proportional to $M_{\rm WD}^{-8}$, where $M_{\rm WD}$ is the mass of the proto-He WD (Chen et al. 2017). In addition, when the WDs enter into the cooling stage, the radii of massive WDs are smaller than those of low-mass WDs with the same effective temperature

[6] In this paper, we mainly consider ELM WDs with masses less than $0.3\,M_{\odot}$, unless otherwise stated. Particularly, we refer to DWDs as binaries consisting of ELM WDs with CO WD companions, which are the most common sources in the ELM Survey.
[7] The term "verification sources" refers to currently known objects from EM observations, which can be individually detected by LISA (Stroeer & Vecchio 2006).
[8] The anticorrelation between the H-rich envelope mass and the WD mass comes from the competition between radiation pressure and gravity pressure around the time of birth of a proto (He or CO) WD. For a massive WD, the nuclear reaction rate of H in the envelope, $\dot{M}_{\rm nuc}$, is high due to the high temperature and density at the bottom of the shell, which leads to a large radiation pressure. When the envelope is small enough, the shell-burning energy can be effectively transferred to the surface and radiate away (Chen et al. 2017). Then, the radiation pressure decreases and can reach equilibrium with the gravity pressure. The timescale of the proto-WD stage can be estimated as $M_{\rm env}/\dot{M}_{\rm nuc}$, where $M_{\rm env}$ is the envelope mass of the proto-WD. There is a positive correlation between $\dot{M}_{\rm nuc}$ and the core mass of the proto-WD, while $M_{\rm env}$ decreases with the proto-WD mass. As a consequence, the timescale in the proto stage is longer for lower WD masses.

(Romero et al. 2019). All of these make the ELM WDs more likely to be discovered by EM observations. In fact, most of the detectable detached DWDs with short orbital periods (<1 day) are those with ELM WD companions. The study of DWDs with ELM WD companions therefore has a significant impact for future space GW detectors.

In general, ELM WDs are mainly produced by binary evolution because the timescale of a single stellar evolution to produce He WDs with mass less than $\sim 0.3\,M_\odot$ is larger than the age of the universe (Kilic et al. 2007). This theoretical result is consistent with the observations that all of the ELM WDs ($\lesssim 0.3\,M_\odot$) are in binary systems (Brown et al. 2016a). Recently, Li et al. (2019) have investigated the formation processes of DWDs with ELM WD companions by combining detailed binary evolution calculations with the BPS method (Paper I hereafter). We show that DWDs with ELM WD companions can be formed from either stable Roche lobe overflow (RL channel) or common envelope (CE) ejection (CE channel). The current local space density is expected to be around 1500 kpc^{-3} for a Milky Way–like galaxy assuming a constant star formation rate (SFR) of 2 $M_\odot\,\mathrm{yr}^{-1}$ (Chomiuk & Povich 2011). This is much larger than the observationally inferred local space density of 160–275 kpc^{-3} (Brown et al. 2016b; Pelisoli & Vos 2019) and needs to be confirmed by future observations.[9] In this paper, with a better Galaxy model, we model the GW radiation (GWR) from Galactic DWDs with ELM WDs, investigate their contributions to the confusion foreground noise, and study the properties of detectable sources with the combination of EM and GW observations.

In current work, we only focus on the detached DWDs. Such systems will become semidetached, and the ELM WDs will become semidetached at some point and the ELM WDs will transfer material to their companions. Because the mass ratios (the ELM WDs to the companions) are around $\sim 1/4$, the mass transfer process is expected to be stable (Han & Webbink 1999), and these binaries resemble AM CVn stars during the mass transfer (Marsh et al. 2004). However, Brown et al. (2016b), by comparing the estimated merger rate of ELM WD binaries with the observed formation rate of AM CVn binaries (see also Brown et al. 2020), argued that the majority of He + CO WDs go through unstable mass transfer and merge into single massive ($\sim 1\,M_\odot$) WDs like R CrB stars. The detailed evolution process between ELM WDs and CO WDs will be discussed in the next paper.

This paper is structured as follows. GW and EM observations are introduced and briefly summarized in Section 2, and the model inputs are given in Section 3. We present the results in Section 4, including chirp mass distribution, foreground noise, resolved sources, chirping sources, and the corresponding results from the combination of EM and GW observations. The uncertainties of our results are presented in Section 5. Finally, we give the summary and conclusion in Section 6.

[9] In Paper I, we adopted a simple assumption of a constant SFR of 2 $M_\odot\,\mathrm{yr}^{-1}$ for our Galaxy. Based on this assumption, the mass of our Galaxy is $2.74 \times 10^{10}\,M_\odot$ at the age of 13.7 Gyr. This SFR is oversimplified, and past SFRs may be larger than 2 $M_\odot\,\mathrm{yr}^{-1}$. In order to better compare with observations, a more realistic model is needed.

2. Observations

2.1. GW Signals of Binary Systems

Only close DWDs ($\lesssim$1 day) could contribute to the confusion foreground noise or be resolved as individual sources by LISA. Due to the strong effect of tidal circularization, we then ignore the eccentric effect of GWR by DWDs and assume that all DWDs have circular orbits. For a DWD binary with an orbital period $P_{\rm orb}$, GWR with a frequency of $f_{\rm GW} = 2/P_{\rm orb}$ takes away the orbital angular momentum and makes the orbit shrink. The rate of orbital angular momentum loss is written as (Landau & Lifshitz 1975)

$$\frac{dJ_{\rm orb}}{dt} = -\frac{32}{5}\frac{G^{7/2}M_1^2M_2^2\sqrt{M_1+M_2}}{c^5a^{7/2}}, \tag{1}$$

where G is the gravitational constant, c is the speed of light in a vacuum, a is the binary separation, and M_1, M_2 are masses of the two stars, respectively. Inserting Kepler's third law into Equation (1), we have

$$\frac{df_{\rm GW}}{dt} = \frac{96}{5}G^{5/3}c^{-5}\pi^{8/3}\mathcal{M}^{5/3}f_{\rm GW}^{11/3}, \tag{2}$$

where $\mathcal{M} = (M_1M_2)^{3/5}(M_1+M_2)^{-1/5}$ is the chirp mass.

For an inspiraling signal, it is convenient to use a characteristic strain, $h_{\rm c}$, which is given by

$$h_c = \sqrt{N_{\rm cycle}}\,\mathscr{A} \tag{3}$$

for monochromatic sources (Finn & Thorne 2000; Moore et al. 2015), where $N_{\rm cycle} = f_{\rm GW}T_{\rm obs}$, $T_{\rm obs}$ is the integration time of the detectors ($T_{\rm obs} = 4$ yr in this work), and $\mathscr{A}$ is the dimensionless GW amplitude, i.e.,

$$\mathscr{A} = \frac{2\pi^{2/3}G^{5/3}f_{\rm GW}^{2/3}\mathcal{M}^{5/3}}{c^4d}, \tag{4}$$

where d is the distance of the binary to the Sun.

To estimate the S/N of sources in LISA, we need to calculate the amplitude of the orbit-averaged detector response, A, which is expressed as (see Equations (42)–(44) of Cornish & Larson 2003)

$$A = \sqrt{|F_+|^2|h_+|^2 + |F_\times|^2|h_\times|^2}, \tag{5}$$

where F_+, $F_\times$ are the detector beam patterns, which depend on the sky location and polarization angle of the source (Cutler 1998; Cornish & Larson 2003; Rubbo et al. 2004; Robson et al. 2018, and references therein). h_+ and $h_\times$ are the two polarizations of a GW signal emitted by a binary (Equation (9)–(10) in Korol et al. 2017). Then, the S/N of a monochromatic periodic source can be calculated by (Moore et al. 2015)

$$\mathrm{S/N}^2 = \int_0^\infty df\frac{4|\tilde{h}(f)^2|}{S_{\rm n}(f)} = \frac{A^2T_{\rm obs}}{S_{\rm n}(f_{\rm GW})}, \tag{6}$$

where $\tilde{h}(f)$ is the Fourier transform of the GW signal as measured by the detector, and $S_{\rm n}(f_{\rm GW})$ is the power spectral density of the detector noise at $f_{\rm GW}$. Here we adopt the current configuration for LISA with a 2.5×10^6 km arm length for the three detector arms, and the total observation time of 4 yr (Amaro-Seoane et al. 2017). The corresponding sensitivity

curve[10] can be found in Robson et al. (2018). The GWR of unresolved binaries will form the galactic confusion noise and can be calculated with the updated version of the BPS model (Nelemans & Tout 2005; Toonen et al. 2012) given in Cornish & Robson (2017). Similar to other studies (e.g., Korol et al. 2017, 2019), we assume that a source could be detected by LISA if the S/N is larger than 7.

2.2. EM Observations

2.2.1. ELM Survey

The ELM Survey is a targeted survey of ELM WDs using dereddened g-band magnitudes ($15 < g_0 < 20$ mag) and color selections to identify targets. It was operated at the 6.5 m MMT telescope (Brown et al. 2010). To obtain a high completeness of follow-up observations, Brown et al. (2016a) defined a "clean" sample of ELM WDs in the following way:

(1) Nonvariable objects are excluded; the semiamplitude is restricted by $k > 75$ km s^{-1} and the orbital period $P_{\rm orb}$ is less than 2 days based on the sensitivity tests.
(2) Surface gravity is in the range of $4.85 < \log g\,({\rm cm\,s^{-2}}) < 7.15$, to ensure the follow-up observations of the ELM Survey are 95% complete.
(3) The color selection provides a built-in temperature selection of $8000 < T_{\rm eff} < 22{,}000$ K.

Finally, there are 62 ELM WDs remaining in the clean sample, where 65% are disk objects and 35% are halo objects from kinematic classification (Brown et al. 2016b, 2020).

The mass distribution of companions of ELM WDs in the clean sample follows a normal distribution with a mean $\mu = 0.76\,M_\odot$ and standard deviation $\sigma = 0.25\,M_\odot$, which suggests CO WD companions for ELM WDs. The ELM WD binary systems in the clean sample have very short orbital periods ($\lesssim$1 day) with a median period of 5.4 hr (Brown et al. 2016a), and about half of these systems will merge in 6 Gyr, due to the GWR (Brown et al. 2016b). In the following, we will explore whether DWDs with ELM WDs in the clean sample have detectable GW signals and how many systems could be discovered by both the ELM Survey and GW detectors.

2.2.2. Gaia Data

Gaia is a full-sky survey with limiting magnitude down to Gaia $m_{\rm G} = 21$ mag (Gaia Collaboration et al. 2016). Gaia Data Release 2 (DR2, Gaia Collaboration et al. 2018) provides precise astrometric and photometric information for billions of sources and gives ~260,000 high-confidence WD candidates (Gentile Fusillo et al. 2019). From Gaia DR2 data, Pelisoli et al. (2019) found 50 new high-probability (pre-)ELM WDs from 3891 subdwarf A-type stars (sdAs[11]), which are previously discovered in the SDSS. This demonstrates that Gaia has the ability to detect more ELM WDs. Based on the known ELM WDs, evolutionary models and the quality control parameters of Lindegren et al. (2018) and Pelisoli & Vos (2019) define a color cut. With this color cut, they get a catalog of 5762 ELM WD candidates from Gaia data. More observations are necessary to confirm these candidates and get their stellar parameters, e.g., log g, $T_{\rm eff}$ (Widmark et al. 2019). In this work, we expect to explore the properties of DWDs containing ELM WDs by combining LISA and Gaia observations.

[10] github.com/eXtremeGravityInstitute/LISA_Sensitivity

[11] Some of the observed properties of sdAs, such as surface gravity and effective temperature, are similar to that of (pre-)ELM WDs. This will lead to some (pre-)ELM WDs being recognized as sdAs (Yu et al. 2019).

3. Model Inputs and Methods

3.1. The Populations of DWDs with ELM WDs in the Galaxy

3.1.1. Parameter Space for Producing ELM WDs from a Detailed Binary Evolution Calculation

In this work, we focus on ELM WD binaries with CO WD companions, which are the most common in the ELM Survey. The formation of such ELM WDs has been systematically investigated in Paper I. We give a brief summary here. The primary in a progenitor binary (initially the more massive one) evolves faster and overfills its Roche lobe on the asymptotic giant branch phase. Then, the primary transfers mass to the secondary. If the mass ratio is large enough, the mass transfer phase is dynamically unstable, and the binary enters into a common envelope (CE) phase. After the ejection of the CE, a CO WD + MS binary is formed. The secondary (The MS companion here) evolves further and fills its Roche lobe at some point. If the secondary starts mass transfer in its late MS or during the Hertzsprung gap (HG) phase, the mass transfer is dynamically stable and a (pre-)ELM WD is produced at the end of mass transfer. This formation channel is called the RL channel. On the contrary, if the secondary starts mass transfer during HG or near the base of the red giant branch (RGB), the mass transfer can be dynamically unstable. Then, the system will enter a CE phase. An ELM WD will be produced after the ejection of the CE, and this formation channel is the CE channel (see Figure 2 in Paper I).

To get the number/birth rate of DWDs with ELM WD components in the Galaxy, we should first know which binary can produce such objects. We then did comprehensive binary evolution calculations, using the state-of-the-art stellar evolution code Modules for Experiments in Stellar Astrophysics (MESA, version 9575; Paxton et al. 2011, 2013, 2015) to obtain the parameter space for producing DWDs with ELM WD components from the RL channel.

Our detailed binary evolution calculations start from binaries consisting of a CO WD and a zero-age main sequence (MS) star. The mass of the CO WD ranges from 0.45 to 1.1 $M_\odot$, and the MS ranges from 0.8 to 2.0 $M_\odot$. The initial orbital period ranges from a minimum period for which the MS star fills its Roche lobe at zero-age MS, and then continues to an upper limit of the orbital period for which the mass transfer rate is up to $10^{-4}\,M_\odot{\rm yr}^{-1}$ (the mass transfer is considered to be dynamically unstable in our calculation) or the He core mass is larger than $0.3\,M_\odot$. We stop our calculation if the evolutionary time is larger than 13.7 Gyr. Such binary evolution calculation for Population I stars with a metallicity of $Z = 0.02$ has been done in Paper I. In the calculation, the mass accumulation efficiency of CO WDs is computed with following formula:

$$\dot{M}_{\rm CO} = \eta_{\rm H}\eta_{\rm He}|\dot{M}_{\rm d}|, \tag{7}$$

where $\eta_{\rm H}$ and $\eta_{\rm He}$ are the mass accumulation efficiencies for hydrogen burning and helium burning, respectively. We adopt the description of Hachisu et al. (1999) and Kato & Hachisu (2004) for $\eta_{\rm H}$ and $\eta_{\rm He}$, respectively.

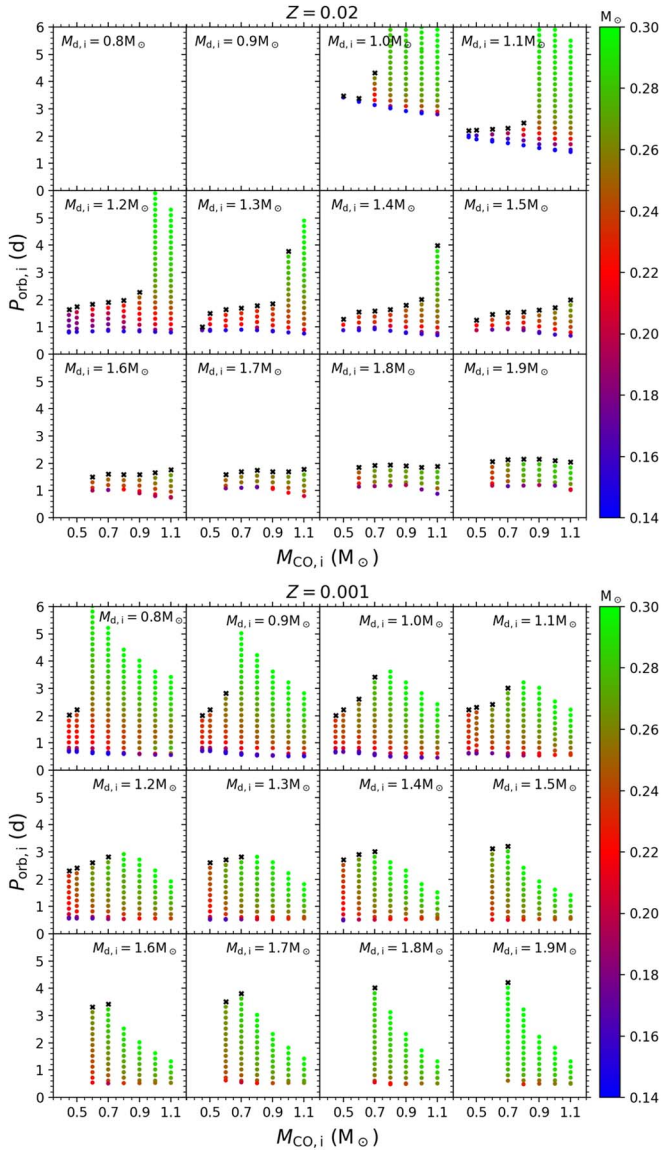

Figure 1. The parameter space for producing ELM WDs from the RL channel of $Z = 0.02$, 0.001 in the CO WD mass–initial orbital period plane ($M_{CO,i} - P_{orb,i}$ plane). The initial donor mass is indicated in each panel. The parameter grids of $M_{d,i} = 2.0\,M_\odot$ are not shown in these two cases. The final masses of ELM WDs are indicated by the color bar. The minimum orbital period is determined by the bifurcation period, and the upper boundary of orbital period is determined by the maximum mass transfer rate of $10^{-4}\,M_\odot\,yr^{-1}$, as shown by the black crosses or the maximum ELM WD mass of $0.3\,M_\odot$.

In order to model the evolution of binaries in the halo, we did the similar binary evolution calculations for $Z = 0.001$ in this paper. The hydrogen mass fraction X is computed as $X = 0.76–3Z$ (Pols et al. 1998). Here we simply assume that the mass accumulation efficiency for $Z = 0.001$ is the same as that for $Z = 0.2$ (see discussion in Meng et al. 2009; Chen et al. 2019).

The parameter spaces for $Z = 0.02$ and $Z = 0.001$ are shown in Figure 1, where $M_{CO,i}$ and $P_{orb,i}$ are the initial CO WD mass and initial orbital period, respectively. The initial donor mass, $M_{d,i}$, is indicated in each panel. The minimum orbital period is determined by the bifurcation period in low-mass binary evolution. If the initial orbital period is shorter than the bifurcation period, the donor star cannot develop a compact He core in its life and evolve to a brown dwarf likely (Chen et al. 2017). The upper boundary of orbital period is determined by the maximum mass transfer rate of $10^{-4}\,M_\odot\,yr^{-1}$ (marked with black crosses) or the maximum helium WDs of $0.3\,M_\odot$. For these plots, we can find that the parameter space for $Z = 0.001$ is obviously larger than that for $Z = 0.02$ for a given MS mass. Furthermore, due to the shorter lifetimes of the low-Z stars, the MS stars with mass as low as $0.8\,M_\odot$ can also contribute to the production of ELM WDs. As a consequence, DWDs with ELM WDs are more likely produced from the RL channel in a low-Z environment than that in the high-Z environment as shown in Section 4.1.

3.1.2. The Populations of ELM WDs in the Galaxy from BPS

To obtain the population of DWDs with ELM WDs in the Galaxy, we first need to produce CO WD binaries from BPS simulations for $Z = 0.02$ (for the bulge and the disk) and $Z = 0.001$ (for the halo), respectively. In the BPS, we need to generate primordial binaries. The main input distributions are introduced below.

(1) SFR. Similar to Yu & Jeffery (2010), we assume a quasi-exponential SFR for the bulge and the disk, i.e.,

$$\mathrm{SFR}(t) = \begin{cases} 10.6\exp^{-(t-t_0)/\tau} \\ \quad +0.125(t-t_0)M_\odot yr^{-1}, & t > t_0 \\ 0, & 0 < t < t_0 \end{cases}. \quad (8)$$

Assuming that the current age of the Galaxy is 13.7 Gyr, $t_0 = 4$ Gyr gives an age of 9.7 Gyr for the bulge and disk. And $\tau = 9$ Gyr yields an SFR of 4.82 $M_\odot\,yr^{-1}$ for the Galaxy, with 1.45 $M_\odot yr^{-1}$ for the bulge and 3.37 $M_\odot yr^{-1}$ for the disk, which are consistent with the observations (Diehl et al. 2006; Fantin et al. 2019).

Regarding the star formation history of the halo, a single starburst with a total mass of $0.7 \times 10^9\,M_\odot$ at $t = 0$ is assumed for the halo (Bland-Hawthorn & Gerhard 2016). Then, we obtain the total mass of the Galaxy, i.e., $M_{Gal} \simeq 6.9 \times 10^{10}\,M_\odot$, and the mass of the bulge, disk, and halo are $2 \times 10^{10}\,M_\odot$, $4.8 \times 10^{10}\,M_\odot$ and $0.7 \times 10^9\,M_\odot$, respectively (see more details in Section 3.2).

(2) Initial mass function IMF. The primary mass is given by the following IMF[12] (Miller & Scalo 1979; Eggleton et al. 1989):

$$M = \frac{0.19X'}{(1-X')^{0.75} + 0.032(1-X')^{0.25}}, \quad (9)$$

where X' is a random number between 0 and 1, which gives the mass ranging from 0.1 to 100 $M_\odot$.

(3) Initial mass ratio distribution (Mazeh et al. 1992):

$$n(q') = 1, \; q' \lesssim 1, \quad (10)$$

where q' represents the mass ratio of the initial binary.

(4) Distribution of initial separation (Han 1998):

$$an(a) = \begin{cases} 0.07(a/a_0)^{1.2}, & a \leqslant a_0 \\ 0.07, & a_0 \leqslant a \leqslant a_1, \end{cases} \quad (11)$$

[12] We have checked the influence of different IMFs on our results and find that about 10% less number of DWDs with ELM WDs are produced if we adopt the IMF from Kroupa (2001).

where $a_0 = 10\,R_\odot$, $a_1 = 5.75 \times 10^6\,R_\odot = 0.13$ pc. This distribution implies that approximately 50% of systems are binary systems with orbital periods less than 100 yr, i.e., the initial binary fraction is assumed to be 50% (see also Han et al. 1995).

For each BPS simulation, we generate 5×10^6 primordial binaries (with $Z = 0.02$ for the disk and bulge, $Z = 0.001$ for the halo) through the Monte Carlo method, then evolve these binaries using the rapid binary-star evolution code BSE (Hurley et al. 2000, 2002) and obtain a number of CO WD binaries in which the companions are just filling their Roche lobes and begin to transfer material to the CO WDs.

In the next step, we interpolate the parameters of CO WD binaries into the corresponding binary evolution grid ($Z = 0.02$,0.001) and obtain the populations of DWDs with ELM WDs from the RL channel.

If a binary has parameters outside of the grid spaces, it either cannot produce an ELM WD or enters the CE evolution phase. The latter can also produce DWDs with ELM WDs as shown in Paper I. We use the standard energy budget prescription to treat this process in BSE. In this prescription, part of the released orbital energy during the spiral-in process is used to eject the envelope[13] (Webbink 1984; Livio & Soker 1988; De Kool 1990). Two parameters, i.e., the CE ejection efficiency $\alpha_{\rm CE}$ and the dimensionless structure parameter λ, are introduced for the energy budget prescription. In Paper I, we adopted three values of the combined parameter $\alpha_{\rm CE}\lambda$ with 0.25, 0.5, and 1, respectively. We find that the model with $\alpha_{\rm CE}\lambda = 1$ can reproduce well the mass peak ($\sim$0.18 $M_\odot$) of the ELM WDs and the mass distribution for the CO WD companions. But the predicted local space density is much higher than that of observations as mentioned in Section 1, indicating that a larger number of DWDs with ELM WDs has not been found yet. In this paper, we adopt $\alpha_{\rm CE}\lambda = 1$ and the effect of the uncertainties of these parameters on our final results is discussed in Section 5.1.

Finally, with the BPS model and the star formation history of the Galaxy, we can simulate the populations of DDs with ELM WDs in the Galaxy.

3.2. The Galaxy Model

The GW strains of binary systems are inversely proportional to the distance. To obtain the distance of each simulated system to the Sun, it is crucial to model the space distribution of stars in the Galaxy. However, the Galaxy structure is very complicated, due to the uncertainty of its star formation history, dynamics, and chemical evolution, etc. (see the most recent review of Bland-Hawthorn & Gerhard 2016). For convenience, here we adopt a spherical power-law model for the bulge, a two-component model for the disk (Binney & Tremaine 2008), and an isotropic double-power-law model for the halo (Kafle et al. 2014). As introduced in Section 3.1.2, the age of the halo (bulge and disk) is assumed to be 13.7 Gyr (9.7 Gyr). The influence of the uncertainties of the Galaxy model on our results is discussed in Section 5.2.

[13] To explain some observed DWDs, Nelemans et al. (2000) suggested an alternative CE ejection mechanism, named the γ-formalism. In this scenario, the orbital angular momentum is carried away by mass loss. However, the physical explanation for γ-formalism is still unclear. Therefore, in this work, we adopt the widely accepted standard energy budget prescription to treat the CE process.

The spatial density of the Galaxy, $\rho_{\rm Gal}$, is written as

$$\rho_{\rm Gal} = \rho_{\rm B} + \rho_{\rm D} + \rho_{\rm H}, \tag{12}$$

where $\rho_{\rm B}$, $\rho_{\rm D}$, and $\rho_{\rm H}$ are the spatial density of the bulge, disk and halo, respectively. The density of the bulge is expressed as

$$\rho_{\rm B}(R, z) = \rho_{\rm B,0} \times \begin{cases} \left(\frac{q}{a_{\rm b}}\right)^{-\alpha_{\rm b}} \exp\left(-\frac{q^2}{r_{\rm b}^2}\right), & q > q_{\rm min}, \\ \left(\frac{q_{\rm min}}{a_{\rm b}}\right)^{-\alpha_{\rm b}} \exp\left(-\frac{q^2}{r_{\rm b}^2}\right), & \text{otherwise}, \end{cases} \tag{13}$$

where (R, z) is the Galactocentric distance and height in cylindrical coordinates, $q = \left(R^2 + \frac{z^2}{q_{\rm b}^2}\right)^{1/2}$, and $\rho_{\rm B,0}$(=1.722 $M_\odot$ pc^{-3}) is the central mass density of the bulge. The cutoff with $q_{\rm min} = 10^{-2}$ kpc is a modification to prevent infinite density at the Galactic center (Astraatmadja & Bailer-Jones 2016). Other values of parameters in the bulge are taken from Binney & Tremaine (2008), i.e., $\alpha_{\rm b} = 1.8$, $a_{\rm b} = 1.0$ kpc, $r_{\rm b} = 1.9$ kpc, and $q_{\rm b} = 0.6$.

For the disk, we have

$$\rho_{\rm D}(R, z) = \frac{\sum_{\rm t}}{2z_{\rm t}} \exp\left(-\frac{R}{R_{\rm t}} - \frac{|z|}{z_{\rm t}}\right) + \frac{\sum_{\rm T}}{2z_{\rm T}} \exp\left(-\frac{R}{R_{\rm T}} - \frac{|z|}{z_{\rm T}}\right), \tag{14}$$

where $\sum_{\rm t} = 970.294\,M_\odot$ pc^{-2} and $\sum_{\rm T} = 268.648\,M_\odot$ pc^{-2} are the central surface densities of the thin and thick disks, respectively. Other values of the parameters in the disk are taken from Bland-Hawthorn & Gerhard (2016), i.e., $R_{\rm t} = 2.6$ kpc, $R_{\rm T} = 2$ kpc, $z_{\rm t} = 0.3$ kpc, and $z_{\rm T} = 0.9$ kpc.

The density of the stellar halo is written as (Kafle et al. 2014),

$$\rho_{\rm H}(r_{\rm G}) = \rho_{\rm H,0} \times \begin{cases} \left(\frac{r_{\rm h,min}}{r_{\rm h,b}}\right)^{-\alpha_{\rm h,1}}, & r_{\rm G} < r_{\rm h,min}, \\ \left(\frac{r_{\rm G}}{r_{\rm h,b}}\right)^{-\alpha_{\rm h,1}}, & r_{\rm h,min} \leqslant r_{\rm G} < r_{\rm h,b}, \\ \left(\frac{r_{\rm h,G}}{r_{\rm h,b}}\right)^{-\alpha_{\rm h,2}}, & r_{\rm h,b} \leqslant r_{\rm G} < r_{\rm h,t}, \\ \left(\frac{r_{\rm h,t}}{r_{\rm h,b}}\right)^{-\alpha_{\rm h,2}} \times \left(\frac{r_{\rm G}}{r_{\rm h,t}}\right)^{\epsilon_{\rm h}} \times \exp\left(-\frac{r_{\rm G} - r_{\rm h,t}}{\triangle_{\rm h}}\right), & r_{\rm G} \geqslant r_{\rm h,t}, \end{cases} \tag{15}$$

where $r_{\rm G}$ is the Galactocentric radius in spherical coordinates and $\rho_{\rm H,0}$(=5.075 $\times$ 10^{-6} $M_\odot$ pc^{-3}) is the central mass density of the halo. The cutoff $r_{\rm h,min} = 0.5$ kpc is to prevent infinite density at the Galactic center. Other values of parameters in the halo are taken from Kafle et al. (2014), i.e., $\alpha_{\rm h,1} = 2.4$, $\alpha_{\rm h,2} = 4.5$, $r_{\rm h,b} = 17.2$ kpc, $r_{\rm h,t} = 97.7$ kpc, $\triangle_{\rm h} = 7.1$ kpc,

Table 1
The Current Birth Rate, Semidetached Rate, Number of DDs in the Galaxy, and the Ratio of DDs from Different Formation Channels to the Total Number

	Bulge	Disk	Halo	Galaxy
$\nu\,(10^{-3})$	2.74	6.56	0.07	9.37
$\xi\,(10^{-3})$	1.78	4.27	0.05	6.10
$N_{\rm tot}\,(10^{7})$	0.63	1.52	0.13	2.18
$\%_{\rm RL}$	65.9%	65.9%	82.8%	67.0%
$\%_{\rm CE}$	34.1%	34.1%	17.2%	33.0%

Note. ν = current birth rate ($\rm yr^{-1}$), ξ = current semidetached rate ($\rm yr^{-1}$), $N_{\rm tot}$ = total number, $\%_{\rm RL}$ and $\%_{\rm CE}$ mean the percentage of the number of systems from the RL and CE channels, respectively.

and $\epsilon_{\rm h} = \frac{r_{\rm h,t}}{\triangle_{\rm h}} - 4.5$. The dark matter components have no effect on our results, so only the baryonic mass is considered in the halo. See Astraatmadja & Bailer-Jones (2016) for further detailed information and discussion.

The position of the Sun is assumed to be $(R_{\rm sun}, z_{\rm sun}) = (8.5\,{\rm kpc}, 16.5\,{\rm pc})$ in cylindrical coordinates (Freudenreich 1998). From the previous section, we can get the current population of DWDs with ELM WDs for different components of the Galaxy. Then we can get the spatial distribution of these binaries according to the spatial density distribution of different components of the Galaxy.

4. Results

4.1. The Number of DDs in the Galaxy

From the simulations in Section 3, we can obtain the population of DWDs with ELM WDs in the Galaxy. The present birth rate ν, semidetached rate ξ, total number $N_{\rm tot}$, the contribution of the RL channel $\%_{\rm RL}$, and that of the CE channel $\%_{\rm CE}$ are shown in Table 1. Here "semidetached rate" means the rate at which the DWDs become semidetached. Then, these DWDs might evolve into AM CVn systems or directly merge into a single star. The total number of DWDs with ELM WD companions at 13.7 Gyr is 2.18×10^{7}. The binary systems from the RL channel could not be resolved/detected by LISA, due to the long orbital periods of such systems ($P_{\rm orb} \gtrsim 0.1$ d, $f_{\rm GW} \lesssim 2 \times 10^{-4}$ Hz). However, some of them would make a contribution to the confusion foreground. For systems from the CE channel, their orbital periods are shorter and more likely to be detected by LISA.

As shown in Table 1, the majority of Galactic DDs with ELM WDs are in the bulge and the disk, where the CE channel contributes more than 30%. However, the contribution of the CE channel in the halo is about half of that in the bulge and disk. We explain this as follows. In comparison to the bulge and disk, due to the low Z of halo stars, the donors (the progenitors of ELM WDs) have large envelope-binding energy and short orbital periods (due to small stellar radius) if they fill their Roche lobes at (or near) the base of the RGB, making it hard to eject the envelope and form ELM WDs consequently (see also Paper I). In addition, as shown in Figure 1, ELM WDs in the halo are more likely produced from the RL channel, due to the relatively large parameter space. Besides, the star formation history also has an effect on this.

We present the galactic age versus the birth rate and semidetached rate for different Galaxy components in Figure 2. The total birth rate and semidetached rate for the disk + bulge ($\nu_{\rm DB,tot}$, $\xi_{\rm DB,tot}$) and the halo ($\nu_{\rm DB,tot}$, $\xi_{\rm DB,tot}$) are shown in the upper panel, while those from the CE channel are presented in the lower panel. In the disk and bulge (exponential SFR), the DWDs with ELM WDs are produced much later than those in the halo, as the SFR defined in Equation (8) indicates that there is no star formation in the first 4 Gyr. Meanwhile, the birth rate is always larger than the semidetached rate for the CE channel (see the thin black solid line and dashed lines in the lower panel), indicating that the number of systems from the CE channel in the disk and bulge increases with age. For the halo, the birth rate and the semidetached rates for ELM WDs from the CE channel are very close. This is a consequence of the fact that a significant part of systems produced from the CE channel in the halo have become semidetached or merged, due to their extremely short orbital periods. This result is consistent with the discussion in Paper I that most halo objects in the ELM Survey are more likely produced from the RL channel (see Figure 11 in Paper I).

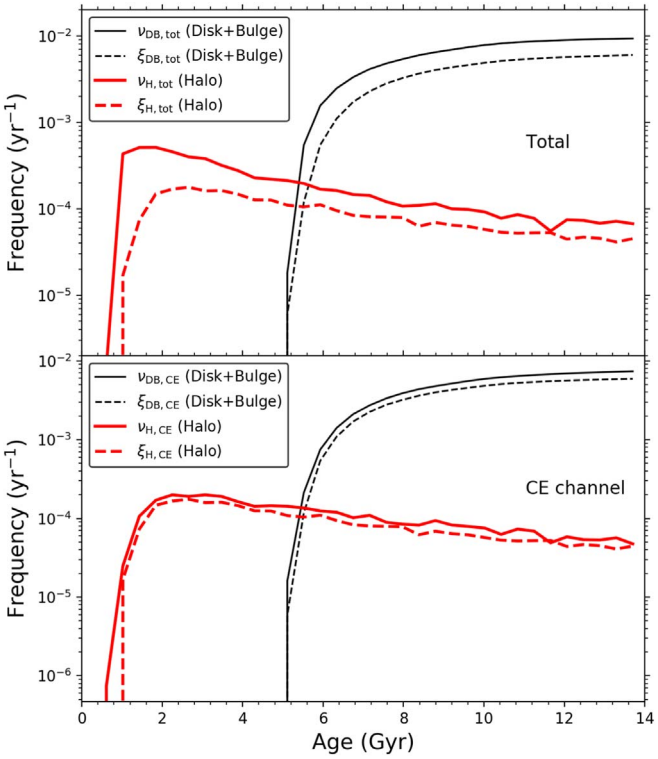

Figure 2. The birth rate and semidetached rate for the Galaxy components, where the bulge and disk are shown together, due to their similar star formation history (exponential SFR; see Section 3.1.2). The total birth rate and semidetached rate are shown in the upper panel, where thin and thick solid lines represent the birth rate for the disk + bulge ($\nu_{\rm DB,tot}$) and the halo ($\nu_{\rm H,tot}$), and the thin and thick dashed lines are for the semidetached rate of the disk + bulge ($\xi_{\rm DB,tot}$) and the halo ($\xi_{\rm H,tot}$), respectively. In the lower panel, we show the corresponding birth rate and semidetached rate of DDs with ELM WDs from the CE channel.

4.2. Chirp Mass

Equation (2) shows that the chirp mass determines the evolution of GW frequency of a binary and could be obtained if the variation of the GW frequency has been detected. We therefore show in Figure 3 the density distribution of the ELM WD mass versus chirp mass (the $M_{\rm He}$–$M_{\rm chirp}$ plane) for Galactic DWDs with ELM WDs. The observed samples are the clean sample in the ELM Survey, which have been divided into two distinct groups according to their formation channels.

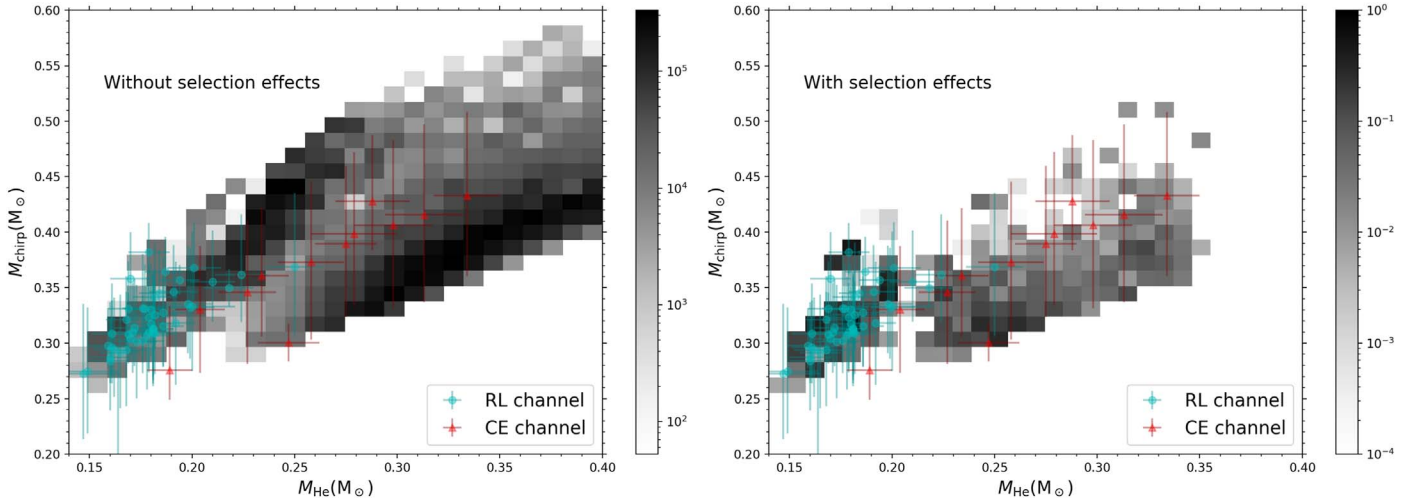

Figure 3. The density distribution in the He WD mass—chirp mass plane for the current population of DDs with ELM WDs in the Galaxy. The left panel shows all of the DDs with ELM companions without considering the selection effects. The ELM WD mass $M_{\rm He}$ peaks around 0.25 and 0.32 $M_\odot$ corresponding to systems from the RL channel and CE channel, respectively. In the right panel, we take the selection effects in the ELM Survey into account, i.e., $k > 75$ km s^{-1}, $P_{\rm orb} < 2$ days, $8000 < T_{\rm eff} < 22{,}000$ K, $4.85 < \log g < 7.15$, and the magnitude limit. About 15% of DDs with ELM WDs ($\sim 3 \times 10^6$) are retained. The two peaks of $M_{\rm He}$ change to 0.18 and 0.25 $M_\odot$, respectively. The observed samples are the clean sample in the ELM Survey, which has been divided into two parts according to the formation channel. The red triangles are for systems produced from the CE channel, and the cyan circles are for those formed from the RL channel.

The red triangles are for those from the CE channel, and the cyan circles are for those from the RL channel. The specific methods to distinguish the formation channel of the observed samples were introduced in Paper I. The basic idea is as follows. We first get a CE efficiency for each sample if we assume that all the observed ELM WDs are from the CE channel. Those with unreasonable values of CE coefficients are considered to be produced from the RL channel, and other samples are supposed to be from the CE channel.

To cover all of the observations, we additionally calculate the parameter spaces for He WDs with mass larger than 0.30 $M_\odot$. The left panel of the figure is for all DDs with ELM WD companions obtained from our calculation, while the right one shows the results with selection effects considered, i.e., $k > 75$ km s^{-1}, $P_{\rm orb} < 2$ days, $8000 < T_{\rm eff} < 22{,}000$ K, $4.85 < \log g < 7.15$, and magnitude limit,[14] as introduced in Section 2.2.1.

From Figure 3, we find that there are two groups of DWDs. The group with typically lower He WD mass is from the RL channel and the other is from the CE channel. The typical chirp mass for the RL channel is comparable to or even slightly larger than that for the CE channel, as the CO WDs from the RL channel can increase its mass during the mass transfer process. After the inclusion of selection effects in the ELM Survey, a large portion of systems with long orbital periods (>2 days) and massive He WDs (large $\log g$ and low $T_{\rm eff}$) are removed. The retained systems are about 15% ($\sim 3 \times 10^6$) of the number without considering the selection effects. Further, the magnitude limit increases the weight of $M_{\rm He} \lesssim 0.2 M_\odot$. We find that the low-mass part matches observations well, while the high-mass part is only marginally consistent with observations. This is possibly caused by the assumption of the envelope mass adopted for ELM WDs produced from the CE channel. As we explained in Paper I, the envelope mass of ELM WDs from the CE channel is likely less massive than that in our study. This means that these WDs should have lower luminosity and larger surface gravity (Calcaferro et al. 2018). Therefore, these systems might not be detected by the ELM Survey because of the magnitude limit or upper limit of surface gravity ($\log g = 7.15$). Of course, our results may also imply that many He WDs with mass larger than $\sim 0.22\, M_\odot$ have not yet been found.

[14] The brighter objects are easier to detect, then we include the magnitude limit by multiplying a weight of $L_{\rm ELM}^{3/2}$, where $L_{\rm ELM}$ is the luminosity of the ELM WDs.

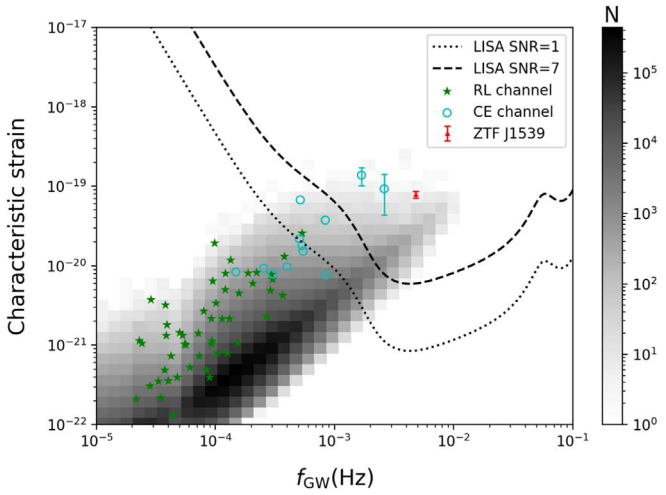

Figure 4. The characteristic GW strains of the current population of DDs with ELM WD companions in the Galaxy. The observed samples from the ELM Survey are shown with green filled stars, and cyan open circles correspond to systems from the RL channel and CE channel, respectively. The dotted and dashed lines are the sensitivity curves with S/Ns = 1 and 7, respectively. The error bars of J0651 and J0935 are taken from Kupfer et al. (2018). ZTF J1539 is an eclipsing DWD system with an orbital period of 6.91 minutes, and its GW strain is taken from Burdge et al. (2019a).

4.3. The GWR Signals of DDs with ELM WDs

Figure 4 shows the GW frequency versus the characteristic strain of DDs with ELM WDs, where the dotted and dashed lines are the all-sky averaged sensitivity curves of LISA when S/Ns = 1 and 7, respectively. The characteristic strains of the

observed samples are also presented in the figure for comparison, and the three with error bars are the potential verification sources for LISA (Kupfer et al. 2018; Burdge et al. 2019a). It is shown that the two distinct populations separated by ELM WD masses in Figure 3 are mixing together and become indistinguishable due to their similar chirp masses and continuous orbital period distribution as shown in the bottom panel of Figure 13 in Paper I. For systems from the RL channel, they generally have large orbital periods, i.e., $f_{\rm GW} \lesssim 10^{-4}$ Hz. On the contrary, the high-frequency region is dominated by DDs from the CE channel.

It appears that the characteristic strain $h_{\rm c}$ from the observed samples is consistent with the theoretical prediction, but is larger than the characteristic strain in the densest region. We verify that the densest region in Figure 4 arises from ELM WDs produced via the CE channel. Due to the uncertainty of the CE process, we assume that the ELM WDs have the same structures as the ones from the RL channel and find that many ELM WDs in DDs with $M_{\rm ELM} \gtrsim 0.22\,M_{\odot}$ are from the CE channel in Paper I. These relatively massive ELM WDs have not been confirmed yet (Pelisoli & Vos 2019), but they are the dominant sources in Figure 4. See also the discussions in Section 4.2.

We confirm that the three most compact systems J0651, J0935, and ZTF J1539 with orbital period about 765 s, 1188 s, and 414 s should be detected by LISA with S/Ns 94, 48, and 130, respectively. These values are close to those in Kupfer et al. (2018) and Burdge et al. (2019a), with S/Ns of 90, 45, and 143, respectively. The minor differences may result from the different sensitivity curves (confusion noise and instrument noise) we adopt. The detailed discussion of the combination of EM and GW observations for the three objects will be presented in Section 4.5. For systems with GW frequency below ∼1 mHz, the GW signals of these binaries will make up the confusion foreground noise (see Section 4.4).

4.4. Foreground Noise and Resolved Sources

To study the GW foreground noise and the resolved sources from DWDs with ELM WDs, we show the GW frequency versus the number distribution of such objects in the upper panel of Figure 5, where the width of each bin is chosen to be $\triangle f_{\rm GW} = 1/T_{\rm obs} = 7.93 \times 10^{-9}$ Hz. Sources are called resolved sources if there is only one individual source in one frequency bin. Here the "resolved sources" only involves the LISA integration time ($T_{\rm obs} = 4$ yr), and whether these sources could be detected by LISA will be discussed below.

We see that the first resolved source appears at $f_{\rm GW} \sim 6 \times 10^{-4}$ Hz, which is smaller than the value (1.5–2.5 mHz) given by Nelemans et al. (2001; see also Ruiter et al. 2010), because (1) we adopt a longer mission time for LISA, i.e., $t_{\rm obs} = 4$ yr instead of 1 yr; (2) we only focus on the DWDs with ELM WDs in this study while Nelemans et al. (2001) were mainly interested in DWDs with relatively massive WDs. We should bear in mind that not all sources with $f_{\rm GW}$ greater than the critical value could be resolved. It can be seen in Figure 5 that there is more than one source in one bin even when $f_{\rm GW} \gtrsim 10^{-3}$ Hz. In this case, the very bright sources in these bins could be extracted from the LISA data (Littenberg 2011).

The number distribution shows two distinct groups with ELM WDs from the RL channel ($f_{\rm GW} \lesssim 10^{-4}$ Hz) and CE channel ($f_{\rm GW} \gtrsim 4 \times 10^{-5}$ Hz), respectively, as shown in the lower panel of Figure 5. The dispersion is very large at 5×10^{-5} Hz ($P_{\rm orb} \sim 0.5$ d) in the total number distribution. This is because the number of ELM WDs from both the RL channel and CE channel at this frequency is very small. In the RL channel, the parameter space to produce systems with orbital period less than ∼0.5 days is very small. Few systems have $f_{\rm GW}$ larger than 5×10^{-5} Hz. In the CE channel, the small number at $f_{\rm GW} \lesssim 5$ mHz is because only ELM WDs with mass larger than $\sim 0.27\,M_{\odot}$ can eject the CE successfully producing systems with final periods $\gtrsim$0.5 days. If we consider the contribution of other types of DWDs, e.g., CO WD + CO WD, the dispersion shown in Figure 5 may be removed (as shown by Yu & Jeffery 2010). A comprehensive study of GWR from the whole DWD population is necessary and will be given in the next paper where we will include recent progress in the study of dynamically instability and the CE evolution in binary evolution as well.

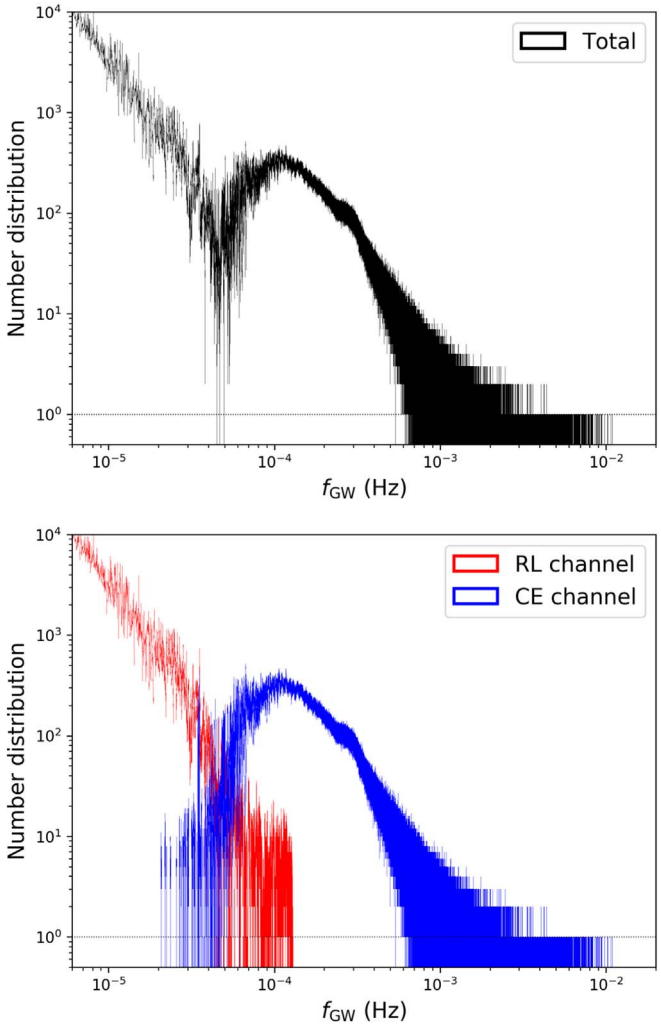

Figure 5. The upper panel shows the number distribution of all ELM DDs in the Galaxy per frequency bin ($\triangle f_{\rm GW} = 1/4\ {\rm yr}^{-1}$), and the contributions from different formation channels are shown in the lower panel. The sources could be resolved for frequency larger than ∼0.6 mHz. The distribution shows two distinct groups with ELM WDs from the RL channel ($f_{\rm GW} \lesssim 10^{-4}$ Hz) and CE channel ($f_{\rm GW} \gtrsim 4 \times 10^{-5}$ Hz), respectively. The dispersion of the number distribution around 5×10^{-5} Hz is caused by the small number of ELM WDs from both channels here. See the text for more details.

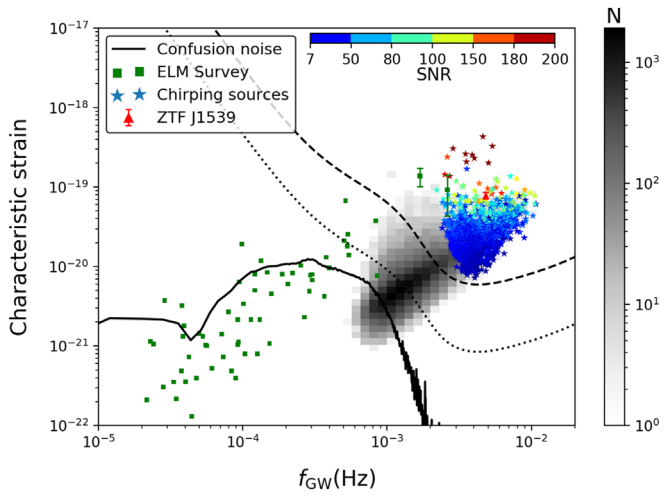

Figure 6. The foreground noise and resolved sources of ELM DDs. The LISA sensitivity curves of S/N = 1, 7 are shown in dotted and dashed lines, respectively. The samples in ELM Survey are shown in green squares. The resolved sources are shown in gray scale, among which 6243 sources are above the LISA sensitivity curve with S/N = 7. The color stars represent the 2023 chirping sources and the colors label the S/N of these systems. The confusion foreground noise is shown by the solid line with a running average of 1000 bins.

In each frequency bin, we calculate the net GW amplitude as in Timpano et al. (2006):

$$h_{\rm net} = \left(\sum_{i=1}^{N_{\rm b}} (h_{\rm c}^2)_i\right)^{1/2}, \tag{16}$$

where $N_{\rm b}$ is the number of sources in each bin. With an average of 1000 bins of the net amplitude, we obtain a smoothing foreground noise shown in Figure 6. In the plot, the distribution of resolved sources is also shown by the gray scale. Both the number of GW sources and individual GW strains determine the shape of the foreground noise. With the increase in $f_{\rm GW}$, the foreground noise remains basically unchanged at $f_{\rm GW} \lesssim 4 \times 10^{-5}$ Hz due to the increase of the GW strains of the individual sources and the decrease of the number of sources (see Figure 5). The dip at $f_{\rm GW} \approx 4.4 \times 10^{-5}$ Hz is caused by the small number of ELM WDs from both channels here, as explained above. Then, the foreground noise increases from $\sim 5 \times 10^{-5}$ Hz to 3×10^{-4} Hz, due to the increase of the GW strains of individual sources, but falls down when $f_{\rm GW} \gtrsim 3 \times 10^{-4}$ Hz because of the sharply decreasing number of GW sources.

We totally obtain 45,735 resolved sources, among which 6243 sources[15] are above the LISA sensitivity curve with S/N = 7. Some resolved sources have very large S/N and could be detected with chirp signals, i.e., the time derivative of the GW frequency $\dot{f}_{\rm GW}$ is larger than the minimum observable chirp $\dot{f}_{\rm GW,min}$, which is written as (Takahashi & Seto 2002; Seto 2002)

$$\begin{aligned} \dot{f}_{\rm GW,min} &\sim C \times \Delta \dot{f}_{\rm GW} \\ &\sim C \times \frac{6\sqrt{5}}{\pi} \frac{1}{T_{\rm obs}^2} \frac{1}{\rm S/N} \\ &\approx 1.3 \times 10^{-17} \left(\frac{100}{\rm S/N}\right) \left(\frac{4{\rm yr}}{T_{\rm obs}}\right)^2 {\rm Hz\ s^{-1}}, \end{aligned} \tag{17}$$

where C was assumed to be 5, meaning that the chirp signal is with 20% accuracy in the LISA measurement (see also Tauris 2018). The colored stars in Figure 6 represent the 2023 chirping sources obtained in our simulation. Different colors in the plot indicate different S/N values. The chirping signals only appear at relatively high GW frequencies (i.e., $f_{\rm GW} \gtrsim 2 \times 10^{-3}$ Hz), mainly due to the high sensitivity of LISA designed in this frequency range and the relatively strong GW strains of individual sources with these frequencies (see Figure 6).

4.5. Combination of EM and GW Observations

We have already shown in Section 4.3 that the three most compact DWDs with ELM WDs would be very likely verified by LISA in the future. This indicates that a few DWDs with ELM WDs could be detected by GW detection and EM observations as well. The combination of GW and EM observations could improve the accuracy of distance measurements and constrain the Galaxy structure further (Shah et al. 2012, 2013; Korol et al. 2019; Littenberg & Cornish 2019). In this section, we discuss EM detections for the detected GW sources of DWDs with ELM WDs.

We consider two projects for EM observations, i.e., the ELM Survey and the Gaia observation. The ELM Survey gives well-defined selection effects of ELM WDs and can be used to test our simulation results. Gaia has the potential to discover an unbiased sample of `LISA` verification sources (Korol et al. 2017) and will give a more complete sample of ELM WDs. In order to get detectable samples of these two projects, we first assume that ELM WDs emit a blackbody spectrum. Then, we redden the flux using the Fitzpatrick (1999) parameterization, where the integrated extinction in the direction of the sources is taken from Schlegel et al. (1998).[16] Finally, we obtain the visual magnitude of the ELM WDs in the SDSS g band (G band for Gaia) for each resolved GW source by using the g-band filter of SDSS (G-band filter of Gaia), as well as the distances obtained by the Galaxy model. For the ELM Survey, we also consider the selection effects introduced in Section 2.2.1. The limiting magnitude is set to 20 for the ELM Survey (Brown et al. 2010) and 21 for Gaia (Gaia Collaboration et al. 2016). Because the 6.5 m MMT is only focusing on the northern sky, we assume that the sources with decl. $> -15°$ could be detected by the ELM Survey for simplicity. There is no sky position limit for Gaia.

Figure 7 shows the sky positions in equatorial coordinates for LISA-detectable sources. The black squares and red crosses represent these sources that are expected to be detected by the ELM Survey and Gaia, respectively. The 62 DWDs with ELM WDs obtained by the ELM Survey are shown with gray filled

[15] The number is slightly larger than that of the recent work of Lamberts et al. (2019) on GWR of DWDs, who found 5600 resolved sources of CO + He WD systems with S/N > 7. The explanation for this difference is due to the different initial binary fraction we used. In this work, systems with orbital periods less than 100 yr are assumed to be binaries. However, Lamberts et al. (2019) assumed that the orbital separation distribution is uniform in log a for $a \leqslant 10^6 R_\odot$, and a binary fraction of 50% was additionally adopted. Consequently, the initial binary fraction in our work is larger than that assumed in Lamberts et al. (2019), which leading to the large number of LISA sources in our results.

[16] These calculations are done with the `Python` package of `dustmaps` (http://argonaut.skymaps.info; Green 2018).

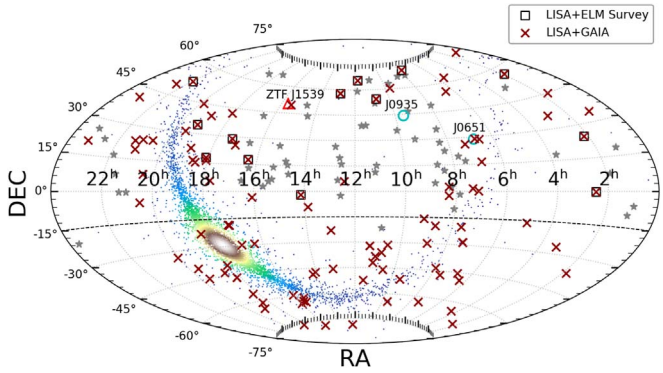

Figure 7. The sky positions of LISA-detectable sources (color dots), and the clean sample of the ELM Survey (gray filled stars). These sources with black squares also satisfy the selection effects in the ELM Survey. These sources with red crosses are expected to be observed by the Gaia space mission. The two cyan open circles and the red open triangle are the verification sources for LISA.

stars for comparison. Almost all GW-detectable sources are in the disk and bulge as expected. Because the objects in the halo are much less than that in the disk and bulge, they are mainly from the RL channel (relatively long orbital period; see Table 1). Therefore, the GW signals from the halo have a negligible effect for LISA detection (see also Ruiter et al. 2009). The expected EM counterparts for those potential GW sources are all in the disk. Although about one-third of the observed samples in ELM Survey are in the halo, these sources are not likely to be detected by LISA. Because most of them are more likely produced from the RL channel due to the relatively longer orbital period ($P_{\rm orb} \gtrsim 0.1$ day) and smaller ELM WD masses ($M_{\rm ELM} \lesssim 0.2\,M_{\odot}$). The expected numbers under different combinations of EM and GW observations are summarized in Table 2.

There are 13 binaries satisfying the selection effects for the ELM Survey, after we limit the observed region to decl. $> -15^{\circ}$. Further, we found that 107 sources have the possibility of being observed by Gaia. More than half (59) of them are in the region of decl. $< 0^{\circ}$. This result is consistent with the discussions in Kupfer et al. (2018) that most LISA verification binaries in the northern hemisphere are caused by the incomplete and biased samples in the observations, and more unbiased sources at low Galactic latitudes are expected to be detected in the future.

We present the characteristic strain of possible candidates from the combination of LISA and Gaia observations in Figure 8, where the green filled squares are the clean samples in the ELM Survey, the black open circles are the sources in our simulations that could be detected by both GW and EM observations, and the black filled stars are for the chirping sources. There are in total 18 sources with measurable chirping signals. According to Equation (17), J0651 and ZTF J1539 have observable chirping signals due to their short orbital periods, but it is hard to detect such a signal for J0935.

Figure 9 shows the distributions of the ELM WD mass, chirp mass, and orbital period for the sources that could be detected by LISA (S/N > 7, the left panels) and the detected sources from the combined observation of LISA and Gaia/ELM Survey (the right panels). From Figure 9, we find that the ELM WD mass distribution peaks around $\sim 0.27\,M_{\odot}$ and the chirp mass distribution peaks around $0.33\,M_{\odot}$. These peaks are located at smaller mass compared with Figure 3. This can be

Table 2
The Statistical Results of LISA Sources

Constraints	Number
LISA	6243
LISA + Chirp	2023
LISA + ELM Survey	13
LISA + Gaia	107
LISA + Gaia + Chirp	18

Note. "LISA" means sources with S/N > 7; "Chirp" means that the sources have measurable chirping signals, and its definition could be found in Section 4.4.

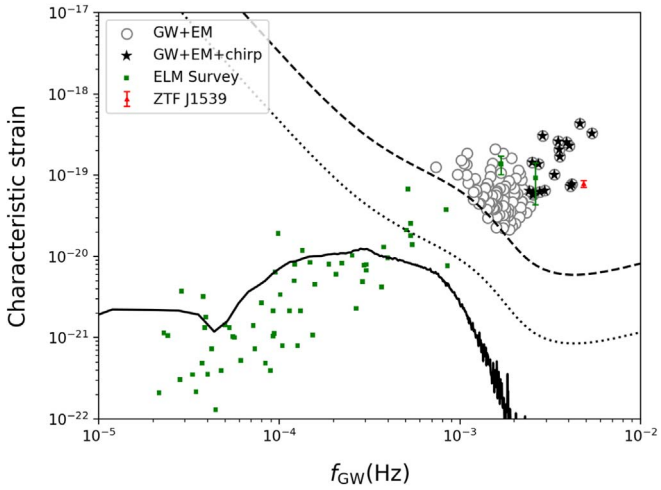

Figure 8. The distribution of possible ELM WDs from the combination of EM (Gaia) and GW observations in $f_{\rm GW}$-characteristic strain plane. The observed samples in the ELM Survey are shown by the green filled squares. The 107 detectable and 18 chirping sources are shown by the gray circles and black stars, respectively.

understood as follows. As shown in Sections 4.3 and 4.4, all the LISA-resolved sources are produced from the CE channel. These sources with larger ELM WD mass and chirp mass have larger orbital periods after the CE process. Then, the GW frequency of these sources is too low to be resolved by LISA.

Most LISA-detectable sources have short orbital periods ($\lesssim$20 minutes) as shown in the lower-left panel. This can be understood as follows. First, the amplitude of GW signals increases with frequency. Therefore, these sources with short orbital periods are more likely to be detected with LISA. Second, LISA is more sensitive to frequency at a few mHZ. Given that the amplitude of GW signals scales as $1/d$ and the amplitude of EM signals scale as $1/d^2$, GW detectors can detect much farther than EM detectors. To see the difference between the EM and GW observations, we make a cutoff at 3.5 kpc (see lower-left panel), which is considered as the maximum observed distance of Gaia (Korol et al. 2017). From this plot, we can find that these sources with shorter orbital periods can be detected by LISA but not EM observations. This explains why these sources detectable with the combination of GW and EM observations have a larger typical orbital period around 20 minutes compared with detectable sources from GW observations.

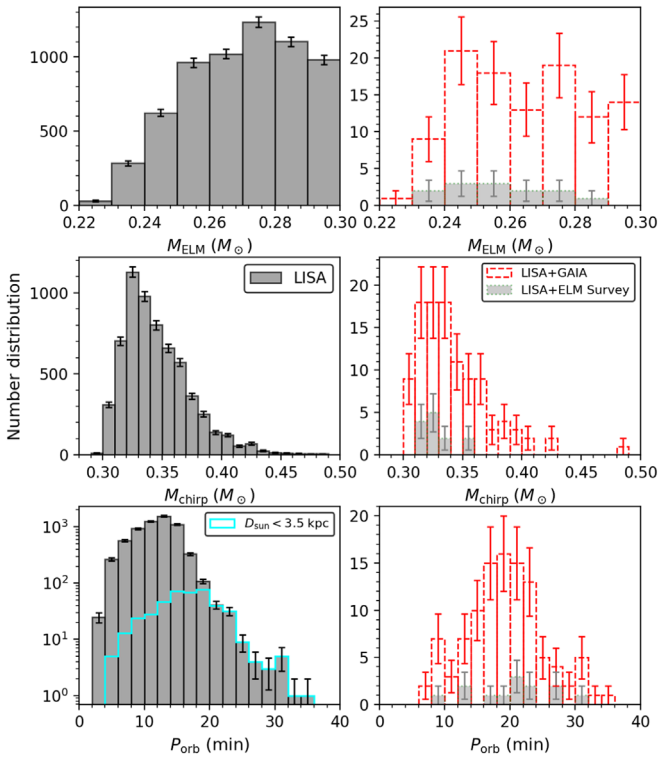

Figure 9. ELM WD mass, chirp mass and orbital period distribution of possibly resolved DWD candidates for LISA observations and combination of EM and GW observations. The LISA sources with distance, $D_{\rm Sun}$, less than 3.5 kpc are shown in the cyan line. The error represents the Poisson error.

Table 3
The Effects of CE Parameters

$\alpha_{\rm CE}\lambda$	$N_{\rm tot}$	$\%_{\rm CE}$	LISA	Chirp	LISA+Gaia
0.25	1.48×10^7	0.2%	382	130	7
0.5	1.47×10^7	5.0%	987	303	18
1	2.18×10^7	34.1%	6243	2023	107

Note. The signs are the same as labeled in Tables 1 and 2.

Table 4
Comparison with a Different Galaxy Model

Galaxy Model	$N_{\rm tot}$	LISA	Chirp	LISA+Gaia
BP99 model	2.92×10^7	4048	1305	72
Fiducial model	2.18×10^7	6243	2023	107

Note. The signs are the same as labeled in Tables 1 and 2.

5. Discussions

5.1. The Uncertainties in the CE Process

One of the main uncertainties of our results comes from the envelope structure of ELM WDs produced from the CE channel, which is still an open question for the CE ejection process. And then we assumed that the envelope structure of these ELM WDs is similar to that of ELM WDs with the same mass from the RL channel. If we overestimate the envelope thickness of ELM WDs from the CE channel, then some systems would not be detected by optical telescopes, due to the large surface gravity and low luminosity (Calcaferro et al. 2018). The combination of EM and GW observations is expected to give a constraint of the envelope structure of ELM WDs from the CE channel. For example, the GW strain contains information about the distance to the sources, which can further help verify the estimates of radius and surface temperature in spectroscopic analysis (Burdge et al. 2019b). These physical quantities are important to infer the lifetime of ELM WDs, which has a strong correlation to the envelope structure of ELM WDs (Althaus et al. 2013; Istrate et al. 2014). It is worth noting that all LISA-resolved sources undergo at least one CE phase (Ruiter et al. 2010; Yu & Jeffery 2010). Therefore, the statistical properties of GW sources can also limit the CE parameters.

The assumption of the CE ejection process has a large effect on our final results. In this work, we adopt the standard energy prescription to simplify this process, with $\alpha_{\rm CE}\lambda = 1$. This parameter value can reproduce the mass distribution of ELM WDs with mass less than $\sim 0.2\,M_\odot$ as well as the companion star mass distribution. Here we test the effect of different parameters in the CE phase, e.g., $\alpha_{\rm CE}\lambda = 0.25$, 0.5. The corresponding results are shown in Table 3. The standard model with $\alpha_{\rm CE}\lambda = 1$ is shown for comparison. We can see that the proportions of systems from the CE channel are strongly correlated with the CE coefficient, because the CE can be ejected more efficiently with larger $\alpha_{\rm CE}\lambda$ (See also Paper I). For the cases of $\alpha_{\rm CE}\lambda = 0.25$ and 0.5, most of the ELM WDs are produced from the RL channel, which has a l0wer contribution to the LISA detection. We find about 382 and 987 sources have S/N larger than 7, and only 7 and 18 systems could be detected by the combination of EM and GW observations for these two cases, respectively.

5.2. The Influence of Galaxy Model on the Results

To test the influence of different Galaxy models on the results, we use similar methods to calculate the GWR of DDs with ELM WD companions in the Galaxy model first suggested by Boissier & Prantzos (1999; which has been developed by Nelemans et al. 2004, BP99 model hereafter). For convenience, we only consider the disk and the bulge components in this model, because the contribution of GWR from the halo populations is expected to be small, as discussed above (see also Ruiter et al. 2009). The total mass of the Galaxy is assumed to be $6.8 \times 10^{10}\,M_\odot$, with bulge mass and disk mass of $2 \times 10^{10}\,M_\odot$ and $4.8 \times 10^{10}\,M_\odot$ for the sake of comparison with the Galaxy model (Fiducial model) assumed in Section 3. The SFR is taken from Boissier & Prantzos (1999), with the SFR doubling in the inner 3 kpc for the bulge (Nelemans et al. 2004, see also Korol et al. 2017). This model gives the Galactic age of 13.7 Gyr, with continuous star formation in the Galaxy history. However, in the fiducial model, the age of the disk and bulge is assumed to be 9.7 Gyr, as shown in Equation (8).

With the BP99 model, we can get 2.92×10^7 DDs with ELM WD companions, 4408 LISA sources, 1305 chirping sources, and 72 candidates for LISA+Gaia observations (see Table 4). Comparing with our fiducial model, we find that the total number of DDs with ELM WD companions in the BP99 model is larger than that in the fiducial model. This difference mainly comes from the different star formation histories in these two models (see also Yu & Jeffery 2013). In the BP99 model, because star formation is continuous over 13.7 Gyr, a considerable portion of ELM WDs are produced from progenitors with mass less than $1.1\,M_\odot$ (with MS lifetime larger than ~ 9 Gyr), which are numerous based on the IMF.

However, in the fiducial model, due to the younger age of the disk and bulge (9.7 Gyr), most ELM WDs are produced from more massive progenitors. Further, for ELM WDs from the CE channel, after the ejection of the CE, the final orbital periods of ELM WDs with low-mass progenitors ($\lesssim 1.1\,M_{\odot}$) are longer compared with those of massive progenitors, which requires more orbital energy from the orbit shrinking to eject the thick envelope. Therefore, in the BP99 model, a relatively lower number of systems could be detected by LISA, as well as the combination with EM observation.

6. Summary and Conclusion

With a hybrid BPS model and the Galaxy model, we have modeled the formation and spatial distribution of DDs with ELM WDs in our Galaxy. We have studied the birth rate and semidetached rate of these systems. In addition, we give a comprehensive discussion about the properties (including chirp mass distribution, frequency distribution) of the population of ELM WDs as GW sources. Finally, we present the properties potential candidates from LISA only and LISA+ELM Survey/Gaia observations. Our main conclusions are summarized as follows.

(1) Most of the halo ELM WDs are produced from the RL channel, which is consistent with the observations. They are hardly detectable by LISA, due to their relatively long orbital periods and low numbers.
(2) There are 400–6000 sources having GW signals higher than the LISA sensitivity curve of $S/N = 7$, among which about 100–2000 have chirping signals.
(3) In the standard model with $\alpha_{\rm CE}\lambda = 1$, about a dozen LISA-detectable sources can possibly be found by the ELM Survey or other ground multiwavelength photometric variability surveys. With the combination of Gaia and LISA, there are about ∼100 sources expected to be detected.
(4) With the combination of EM and GW observations, ELM WDs with mass $\lesssim 0.27\,M_{\odot}$ have a large possibility of being detected, the chirp masses for those systems are generally less than $\sim 0.4\,M_{\odot}$, and the orbital period distribution shows the mean value around ∼22 minutes.

We thank the anonymous referee for very helpful suggestions on the manuscript. The authors would like to thank Valeriya Korol for providing the table of star formation rates for the BP99 Galactic model. The authors gratefully acknowledge the computing time granted by the Yunnan Observatories and provided for the facilities at the Yunnan Observatories Supercomputing Platform. This work is partially supported by the Natural Science Foundation of China (grant Nos. 11733008, 11521303, 11703081, 11422324), by the National Ten-thousand talents program, by Yunnan province (No. 2017HC018), by the Youth Innovation Promotion Association of the Chinese Academy of Sciences (grant No. 2018076), and the CAS Light of West China Program.

Software: BSE (Hurley et al. 2000, 2002). MESA (v9575; Paxton et al. 2011, 2013, 2015).

ORCID iDs

Zhenwei Li https://orcid.org/0000-0002-1421-4427

References

Althaus, L. G., Miller Bertolami, M. M., & Córsico, A. H. 2013, A&A, 557, A19
Amaro-Seoane, P., Aoudia, S., Babak, S., et al. 2013, GW Notes, 6, 4
Amaro-Seoane, P., Audley, H., Babak, S., et al. 2017, arXiv:1702.00786
Astraatmadja, T. L., & Bailer-Jones, C. A. L. 2016, ApJ, 832, 137
Baker, J., Haiman, Z., Rossi, E. M., et al. 2019, BAAS, 51, 123
Binney, J., & Tremaine, S. 2008, Galactic Dynamics (2nd ed.; Princeton, NJ: Princeton University Press)
Bland-Hawthorn, J., & Gerhard, O. 2016, ARA&A, 54, 529
Boissier, S., & Prantzos, N. 1999, MNRAS, 307, 857
Brown, W. R., Gianninas, A., Kilic, M., Kenyon, S. J., & Allende Prieto, C. 2016a, ApJ, 818, 155
Brown, W. R., Kilic, M., Allende Prieto, C., Gianninas, A., & Kenyon, S. J. 2013, ApJ, 769, 66
Brown, W. R., Kilic, M., Allende Prieto, C., & Kenyon, S. J. 2010, ApJ, 723, 1072
Brown, W. R., Kilic, M., Allende Prieto, C., & Kenyon, S. J. 2012, ApJ, 744, 142
Brown, W. R., Kilic, M., Hermes, J. J., et al. 2011, ApJL, 737, L23
Brown, W. R., Kilic, M., Kenyon, S. J., & Gianninas, A. 2016b, ApJ, 824, 46
Brown, W. R., Kilic, M., Kosakowski, A., et al. 2020, ApJ, 889, 49
Burdge, K. B., Coughlin, M. W., Fuller, J., et al. 2019a, Natur, 571, 528
Burdge, K. B., Fuller, J., Phinney, E. S., et al. 2019b, ApJL, 886, L12
Calcaferro, L. M., Althaus, L. G., & Córsico, A. H. 2018, A&A, 614, A49
Carrasco, J. M., Catalán, S., Jordi, C., et al. 2014, A&A, 565, A11
Chen, H.-L., Woods, T. E., Yungelson, L. R., et al. 2019, MNRAS, 490, 1678
Chen, X., Maxted, P. F. L., Li, J., & Han, Z. 2017, MNRAS, 467, 1874
Chomiuk, L., & Povich, M. S. 2011, AJ, 142, 197
Cooray, A., Farmer, A. J., & Seto, N. 2004, ApJL, 601, L47
Cornish, N., & Robson, T. 2017, JPhCS, 840, 012024
Cornish, N. J., & Larson, S. L. 2003, PhRvD, 67, 103001
Cutler, C. 1998, PhRvD, 57, 7089
De Kool, M. 1990, ApJ, 358, 189
Diehl, R., Halloin, H., Kretschmer, K., et al. 2006, Natur, 439, 45
Eggleton, P. P., Fitchett, M. J., & Tout, C. A. 1989, ApJ, 347, 998
Evans, C. R., Iben, I. J., & Smarr, L. 1987, ApJ, 323, 129
Fantin, N. J., Côté, P., McConnachie, A. W., et al. 2019, ApJ, 887, 148
Finn, L. S., & Thorne, K. S. 2000, PhRvD, 62, 124021
Fitzpatrick, E. L. 1999, PASP, 111, 63
Freudenreich, H. T. 1998, ApJ, 492, 495
Gaia Collaboration, Babusiaux, C., van Leeuwen, F., et al. 2018, A&A, 616, A10
Gaia Collaboration, Prusti, T., de Bruijne, J. H. J., et al. 2016, A&A, 595, A1
Gentile Fusillo, N. P., Tremblay, P.-E., Gänsicke, B. T., et al. 2019, MNRAS, 482, 4570
Gianninas, A., Kilic, M., Brown, W. R., Canton, P., & Kenyon, S. J. 2015, ApJ, 812, 167
Hachisu, I., Kato, M., & Nomoto, K. 1999, ApJ, 522, 487
Han, Z. 1998, MNRAS, 296, 1019
Han, Z., Podsiadlowski, P., & Eggleton, P. P. 1995, MNRAS, 272, 800
Han, Z., & Webbink, R. F. 1999, A&A, 349, L17
Hermes, J. J., Kilic, M., Brown, W. R., et al. 2012, ApJL, 757, L21
Hurley, J. R., Pols, O. R., & Tout, C. A. 2000, MNRAS, 315, 543
Hurley, J. R., Tout, C. A., & Pols, O. R. 2002, MNRAS, 329, 897
Istrate, A. G., Tauris, T. M., Langer, N., & Antoniadis, J. 2014, A&A, 571, L3
Kafle, P. R., Sharma, S., Lewis, G. F., & Bland-Hawthorn, J. 2014, ApJ, 794, 59
Kato, M., & Hachisu, I. 2004, ApJL, 613, L129
Kilic, M., Brown, W. R., Allende Prieto, C., et al. 2011, ApJ, 727, 3
Kilic, M., Brown, W. R., Allende Prieto, C., et al. 2012, ApJ, 751, 141
Kilic, M., Stanek, K. Z., & Pinsonneault, M. H. 2007, ApJ, 671, 761
Korol, V., Rossi, E. M., & Barausse, E. 2019, MNRAS, 483, 5518
Korol, V., Rossi, E. M., Groot, P. J., et al. 2017, MNRAS, 470, 1894
Kroupa, P. 2001, MNRAS, 322, 231
Kupfer, T., Korol, V., Shah, S., et al. 2018, MNRAS, 480, 302
Lamberts, T., Blunt, A., Littenberg, S., et al. 2019, MNRAS, 490, 5888
Landau, L. D., & Lifshitz, E. M. 1975, The Classical Theory of Fields (New York, Oxford: Pergamon Press)
Li, Z., Chen, X., Chen, H.-L., & Han, Z. 2019, ApJ, 871, 148
Lindegren, L., Hernández, J., Bombrun, A., et al. 2018, A&A, 616, A2
Littenberg, T. B. 2011, PhRvD, 84, 063009
Littenberg, T. B., & Cornish, N. J. 2019, ApJ, 881, 43
Littenberg, T. B., Larson, S. L., Nelemans, G., & Cornish, N. J. 2013, MNRAS, 429, 2361

Liu, J. 2009, MNRAS, 400, 1850
Liu, J., Han, Z., Zhang, F., & Zhang, Y. 2010, ApJ, 719, 1546
Livio, M., & Soker, N. 1988, ApJ, 329, 764
LSST Science Collaboration, Abell, P. A., Allison, J., et al. 2009, arXiv:0912.0201
M. Green, G. 2018, JOSS, 3, 695
Marsh, T. R., Nelemans, G., & Steeghs, D. 2004, MNRAS, 350, 113
Mazeh, T., Goldberg, D., Duquennoy, A., & Mayor, M. 1992, ApJ, 401, 265
Meng, X., Chen, X., & Han, Z. 2009, MNRAS, 395, 2103
Miller, G. E., & Scalo, J. M. 1979, ApJS, 41, 513
Moore, C. J., Cole, R. H., & Berry, C. P. L. 2015, CQGra, 32, 015014
Nelemans, G. 2006, in AIP Conf. Ser. 873, Laser Interferometer Space Antenna: 6th Int. LISA Symp., ed. S. M. Merkovitz & J. C. Livas (Melville, NY: AIP), 397
Nelemans, G., & Tout, C. A. 2005, MNRAS, 356, 753
Nelemans, G., Verbunt, F., Yungelson, L. R., & Portegies Zwart, S. F. 2000, A&A, 360, 1011
Nelemans, G., Yungelson, L. R., & Portegies Zwart, S. F. 2001, A&A, 375, 890
Nelemans, G., Yungelson, L. R., & Portegies Zwart, S. F. 2004, MNRAS, 349, 181
Nissanke, S., Vallisneri, M., Nelemans, G., & Prince, T. A. 2012, ApJ, 758, 131
Paxton, B., Bildsten, L., Dotter, A., et al. 2011, ApJS, 192, 3
Paxton, B., Cantiello, M., Arras, P., et al. 2013, ApJS, 208, 4
Paxton, B., Marchant, P., Schwab, J., et al. 2015, ApJS, 220, 15
Pelisoli, I., Bell, K. J., Kepler, S. O., & Koester, D. 2019, MNRAS, 482, 3831
Pelisoli, I., & Vos, J. 2019, MNRAS, 488, 2892
Pols, O. R., Schröder, K.-P., Hurley, J. R., Tout, C. A., & Eggleton, P. P. 1998, MNRAS, 298, 525
Robson, T., Cornish, N., & Liu, C. 2018, CQG, 36, 105011
Romero, A. D., Kepler, S. O., Joyce, S. R. G., Lauffer, G. R., & Córsico, A. H. 2019, MNRAS, 484, 2711
Rubbo, L. J., Cornish, N. J., & Poujade, O. 2004, PhRvD, 69, 082003
Ruiter, A. J., Belczynski, K., Benacquista, M., & Holley-Bockelmann, K. 2009, ApJ, 693, 383
Ruiter, A. J., Belczynski, K., Benacquista, M., Larson, S. L., & Williams, G. 2010, ApJ, 717, 1006
Schlegel, D. J., Finkbeiner, D. P., & Davis, M. 1998, ApJ, 500, 525
Seto, N. 2002, MNRAS, 333, 469
Shah, S., & Nelemans, G. 2014a, ApJ, 790, 161
Shah, S., & Nelemans, G. 2014b, ApJ, 791, 76
Shah, S., Nelemans, G., & van der Sluys, M. 2013, A&A, 553, A82
Shah, S., van der Sluys, M., & Nelemans, G. 2012, A&A, 544, A153
Stroeer, A., & Vecchio, A. 2006, CQGra, 23, S809
Takahashi, R., & Seto, N. 2002, ApJ, 575, 1030
Tauris, T. M. 2018, PhRvL, 121, 131105
Timpano, S. E., Rubbo, L. J., & Cornish, N. J. 2006, PhRvD, 73, 122001
Toonen, S., Nelemans, G., & Portegies Zwart, S. 2012, A&A, 546, A70
Webbink, R. F. 1984, ApJ, 277, 355
Webbink, R. F., & Han, Z. 1998, in AIP Conf. Ser. 456, Laser Interferometer Space Antenna, Second Int. LISA Symp. on the Detection and Observation of Gravitational Waves in Space, ed. W. M. Folkner (Melville, NY: AIP), 61
Widmark, A., Mortlock, D. J., & Peiris, H. V. 2019, MNRAS, 485, 179
Yu, J., Li, Z., Zhu, C., et al. 2019, ApJ, 885, 20
Yu, S., & Jeffery, C. S. 2010, A&A, 521, A85
Yu, S., & Jeffery, C. S. 2013, MNRAS, 429, 1602